Materials Advances

ROYAL SOCIETY OF CHEMISTRY

PAPER

View Article Online
View Journal | View Issue

Cite this: *Mater. Adv.*, 2024, 5, 6572

Insights into the development and performance of $CuO/CuFe_2S_xO_{4-x}$ catalysts: an effective approach for renewable hydrogen generation†

Ejaz Hussain, *[a] Muhammad Jalil,[a] Muhammad Zeeshan Abid,[a] Javeria Mansab,[a] Raed H. Althomali,[b] Shuxin Wang,[c] Abdul Rauf[a] and Khezina Rafiq *[a]

Hydrogen is an ideal alternative to fossil fuels owing to its renewable, carbon-free, high-energy-mass, and sustainable nature. The aim of this study was to develop a cost-effective and sustainable approach for green fuel (H_2) production. To achieve this objective, $CuO/CuFe_2S_xO_{4-x}$ catalysts were synthesized and employed for photoreaction to generate hydrogen. For achieving progressive results, a hydrothermal approach was used to synthesize the catalysts. XRD analysis confirmed that sulphur doping causes lattice strain through the incorporation of larger sulphur anions. SEM results revealed that sulphur doping has reduced agglomeration to increase active sites for hydrogen evolution. Electrochemical and photoluminescence studies demonstrated that presence of sulphur dopants and CuO promote charge separation and transfer of photogenerated charges to the reaction sites and facilitate water reduction reactions for H_2 production. Moreover, the CuO content improved the oxidation potential of $CuFe_2S_xO_{4-x}$ catalysts. EDX and XPS analyses verified the elemental compositions and oxidation states of the catalysts, while VSM and EPR results confirmed the improved magnetic and electronic properties that are expected to enhance the photocatalytic activity. Overall, $CuO/CuFe_2S_xO_{4-x}$ generated 7.45 mmol g^{-1} h^{-1} of hydrogen with an AQY of 2.45%, that was five times higher than pristine $CuFe_2O_4$. On the basis of results, it could be concluded that $CuO/CuFe_2S_xO_{4-x}$ catalysts can potentially be utilized for green fuel (H_2) generation applications.

Received 17th December 2023,
Accepted 5th July 2024

DOI: 10.1039/d3ma01137b

rsc.li/materials-advances

Introduction

Environmental pollution due to burning of fossil fuels has become an important global issue. In the modern era, the growth of industrialization has led to a significant increase in harmful pollutants.[1] The traditional sources of energies, including petroleum, gas, and coal, that are commonly used in industries, vehicles and airplanes, are major concerns owing to their widespread usage across the world. It is worth mentioning that pollutants such as CO_x, SO_x, and NO_x emitted from these fossil fuels have been found to be carcinogenic and harmful.[2,3] Moreover, owing to the large consumption, fossil fuel resources are declining day by day. Thus, there is an urgent need for sustainable alternatives that can not only meet the energy needs but also are environmentally friendly. For this purpose, researchers are working to develop new catalysts that can be efficiently used for the synthesis of green fuels (hydrogen) as alternatives. Hydrogen is one of the sustainable fuels that can not only fulfil the energy demands but can also help resolve environmental pollution.[4] Although there are different ways to generate hydrogen, one of the most promising approaches is the production of hydrogen *via* photocatalytic reactions.[5]

Catalysts play a vital role in the photocatalytic water-splitting reaction, and there are several materials that behave like catalysts, but they are not stable or cost effective.[6,7] Hence, further study is needed to establish economical, environmentally friendly, and stable catalysts that can overcome these challenges. Numerous materials have been explored for this purpose, such as metal oxides,[8] sulphides,[9–11] metal nanoparticles,[12] metallic and non-metallic materials,[13] MXene-based materials,[14,15] gold-supported catalysts,[16] vanadates,[17] and transition metal ferrites.[18] Among these materials, nanomaterials based on

[a] *Institute of Chemistry, Inorganic Materials Laboratory 52S, The Islamia University of Bahawalpur, 63100, Pakistan. E-mail: ejaz.hussain@iub.edu.pk, khezina.rafiq@iub.edu.pk*
[b] *Department of Chemistry, College of Arts and Science, Prince Sattam Bin Abdulaziz University, Wadi Al-Dawasir–11991, Saudi Arabia*
[c] *College of Materials Science and Engineering, Qingdao University of Science and Technology, Qingdao–266042, P. R. China*

† Electronic supplementary information (ESI) available. See DOI: https://doi.org/10.1039/d3ma01137b

transition metal ferrites exhibit desirable characteristics, including large surface area, affordability, extraordinary stability, and excellent catalytic features.[19] These attributes make transition metal ferrites particularly appealing for photocatalytic applications.

In the field of photocatalysis, various ferrites, including spinel ferrites, have been widely investigated and utilized as catalysts. Spinel ferrites belong to the class of compounds of the type $M^{2+}M_2{}^{3+}O_4$, and have attracted significant attention in photocatalytic studies.[20] Their unique properties and composition make them highly suitable for catalytic applications. Indeed, the general formula for spinel ferrites is MFe_2O_4, where M represents a divalent metal ion, such as zinc, manganese, nickel, copper, and others. The specific structure and alignment of ferrites play a crucial role in their adsorption capabilities.[21] Factors such as their morphology and inherent crystal structure directly impact their ability to adsorb substances.[22] The diverse characteristics of ferrites allow variations in their adsorption properties, making them adaptable for various applications in the field of photocatalysis.[23] $CuFe_2O_4$ is indeed a spinel-type material that exhibits several desirable properties for the water-splitting reaction. Its band gap is narrow, which enables it to be active under solar light, enhancing its photochemical stability and efficiency.[24] Additionally, $CuFe_2O_4$ is known for its cost-effectiveness, adaptability, and non-toxicity, further adding to its appeal as a catalyst for the water-splitting reaction.[25] Its combination of beneficial characteristics makes $CuFe_2O_4$ an attractive candidate for various applications related to the photocatalysis and treatment of water resources. Several methods have been reported for synthesizing microstructures of spinel ferrites, including sol–gel, photo and electro deposition, solid-state reaction, hydrothermal, and coprecipitation methods.[26] Among these methods, the hydrothermal approach is favoured due to its versatility, capacity to produce uniform structures, and high purity of the synthesized materials.[27] The hydrothermal method is particularly advantageous for its ability to achieve versatility, uniformity, and purity in the resulting spinel ferrite microstructures, making it the preferred choice for the synthesis of catalysts.[28]

Various techniques have been utilized to enhance the photocatalytic efficiencies of $CuFe_2O_4$, including the construction of nanocomposites, the formation of Schottky barriers, and doping with various elements.[29] The selective incorporation of metals play an important role in modifying the band structure, resulting in the generation of quasi-stable energy levels.[30] These strategies aim to enhance the overall performance of $CuFe_2O_4$ as a photocatalyst. Recent studies have focused on introducing sulphur dopants into different materials, such as g-C_3N_4, graphene sheets, and ZnO, to enhance their photocatalytic applications.[31] The incorporation of sulphur dopants leads to modifications in the electrical and photocatalytic properties of these oxides.[32] Several researchers have reported that $CuFe_2O_4$ can split water but with a lower AQY because its oxidation potential is not favourable for water oxidation. For water splitting, the oxidation potential must be greater than 1.23 eV, but $CuFe_2O_4$'s oxidation potential is 1.03 eV, which does not favour water splitting.[33] For this purpose, we introduced CuO (oxidation potential of 2.25 eV) in $CuFe_2O_4$ to helps in the water oxidation. By incorporating sulphur dopants, it becomes possible to tailor and improve the performance of materials in various photocatalytic processes. CuO was also present in very low amount and it enhances the oxidation potential of $CuO/CuFe_2S_xO_{4-x}$ cocatalysts for the water-splitting reaction.[34,35]

In order to harvest the benefits of S-dopants in conventional ferrites, hydrothermal treatment was employed here to prepare $CuO/CuFe_2S_xO_{4-x}$ photocatalysts. These catalysts were prepared and utilized for H_2 production in the presence of sunlight. The results clearly indicate that $CuO/CuFe_2S_xO_{4-x}$ had superior photocatalytic efficiency compared to pristine $CuFe_2O_4$.

Experimental

Chemicals

Copper nitrate (Sigma Aldrich CAS No 10031-43-3), iron nitrate (Sigma Aldrich CAS No 7782-61-8), glucose (Sigma CAS No 50-99-7), thiourea (Sigma CAS No 62-56-6), C_2H_5OH (Sigma CAS No 64-17-5), sodium hydroxide (Sigma CAS No 1310-73-2), and deionized water were used for preparation of the catalysts.

Catalyst preparation

The synthesis of copper ferrites using the hydrothermal method followed the following procedure: initially, solutions containing 0.2 M $Cu(NO_3)_2{\cdot}5H_2O$ and 0.4 M $Fe(NO_3)_3$ were magnetically agitated for a duration of 30 min. The preparation of the solutions is described in the ESI.† Subsequently, 0.01 M glucose solution was added to the above mixture, which was then left to stir for 22 h at a temperature of 50 °C. Once the mixture solution was obtained, it was sonicated for 30 min at a sweep frequency of approximately 37 kHz using a 300 W bath sonicator. The resulting solution was transferred to an autoclave reactor and the temperature was maintained at 140 °C for a duration of 6 h. (Note: for the synthesis of the $CuO/CuFe_2O_4$ catalysts, 2% w/w CuO was also added in the reaction mixture before starting the hydrothermal reaction). After the completion of the reaction, the solution was allowed to cool down and was then filtered using high-grade filter paper. The precipitates were washed thoroughly with an ethanol–water mixture and calcined at 400 °C, yielding 85% $CuFe_2O_4$ and 83% $CuFe_2O_4$/CuO, respectively. For the synthesis of ($CuO/CuFe_2S_xO_{4-x}$), 500 mg of $CuFe_2O_4$ and 10 mg (2% w/w) of CuO were transferred to a Teflon-lined autoclave reactor. For sulphur incorporation, 1% (w/w) of sulphur contents sourced *via* thiourea was mixed with $CuFe_2O_4$, which was then placed back in the autoclave for 6 h at 140 °C. After that, the $CuO/CuFe_2S_xO_{4-x}$ catalysts were filtered, dried, and after calcination an 82% yield was obtained.[36,37] The synthesis scheme for the photocatalysts is demonstrated in Fig. 1.

Characterization

Various analytical techniques were used to characterize the $CuO/CuFe_2S_xO_{4-x}$ catalysts. Powder X-ray diffraction (PXRD)

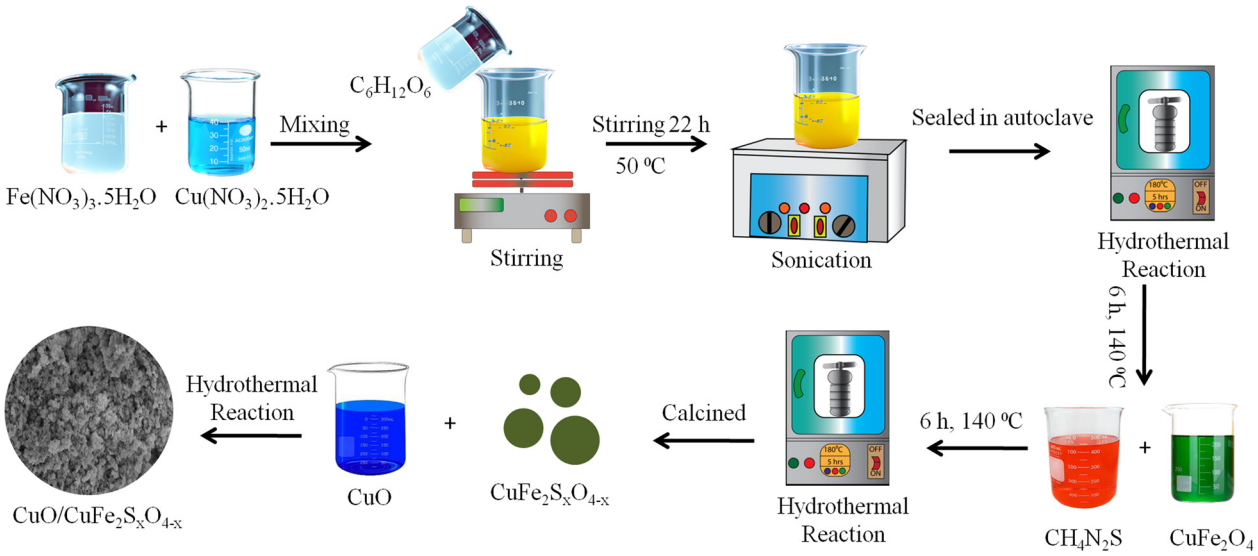

Fig. 1 Synthesis scheme for $CuO/CuFe_2S_xO_{4-x}$ catalysts.

analysis was conducted using a Philips-X Pertpro instrument equipped with Cu kα radiation (λ = 1.5406 Å). The surface morphology of the synthesized catalysts was examined using scanning electron microscopy (SEM) with a field emission scanning electron microscopy system (FESEM, FEI-Nova Nano SEM-450). The chemical composition analysis of the prepared catalysts was performed using energy dispersive X-ray analysis (EDX) employing a Horiba 7593 H instrument. A PARK NX10 instrument was used for AFM analysis of the catalysts. For measurement of the optical properties, ultraviolet-vi-DRS analysis was conducted. Photoluminescence (PL) measurements were performed on a Hitachi F-4600 fluorescence spectrometer. The emission spectra were recorded in the range of 350–670 nm with an excitation wavelength of 300 nm. Excitation and emission slit widths of 5 nm were used. A catalyst amount of 10 mg was employed for all the measurements. A TG-209 F3 Tarsus instrument was used for the TGA analysis. FTIR and Raman analyses were performed on Bruker and JASCO spectrometers, respectively. A PHOIBOS electron energy analyzer from SPECS GmbH, with a Mg Kα electron source with a base pressure of less than 1×10^{-9}, was used for the XPS measurements. A Tristar II (3020) BET analyzer was used to measure the N_2 adsorption and desorption curves. VSM was performed on a high field measurement system based on closed-cycle/cryogen-free technology. The EPR studies were performed on a Bruker Elexsys-II-E500-CW instrument.

Photocatalytic reactions

To assess the photocatalytic hydrogen-generation performances, the synthesized catalysts were tested under visible-light irradiation using a quartz reactor. A GC-TCD (Shimadzu-2010) system was utilized to quantify the hydrogen. Visible-light irradiation was provided by a 100 W halogen lamp emitting light with a wavelength (λ) greater than 400 nm. For each photoreaction, the following conditions were utilized: 10 mg photocatalyst, pH 8, 5% ethanol sacrificial reagent, and a duration of 6 h. During the experiment, the light source was positioned 25 cm away from the reaction mixture. The efficiency of the catalysts for hydrogen generation was evaluated at regular time intervals. The hydrogen-generation rate was measured in mmol g^{-1} h^{-1} and mmol g^{-1} [38] and the quantum efficiency was calculated by the following formula.[39]

$$\text{Quantum efficiency} = \frac{\text{mole of } H_2 \text{ produced}}{\text{number of photon absorbed}} \times 100$$

Results and discussion

The synthesis procedure for the $CuO/CuFe_2S_xO_{4-x}$ photocatalysts is illustrated in Fig. 1, and is comprehensively explained in the "Experimental" section of this paper. For the removal of impurities and for improving the crystallinity, the as-synthesized products underwent a calcination process at a temperature of 450 °C for a duration of 3 h. This calcination step aimed to improve the structural properties and morphology of the photocatalysts to ensure their optimal performance in subsequent photocatalytic applications.

X-Ray diffraction (XRD) analysis

The crystalline nature and phase purity of the synthesized catalysts were analyzed by X-ray diffraction analysis. The XRD patterns of the copper ferrite nanostructures are depicted in Fig. 2(a). The observed diffraction peaks corresponded well to the JCPDS card No. 77-0010. The characteristic positions of the prepared product were observed at 18.34°, 30.17°, 35.54°, 43.19°, 53.59°, 57.13°, and 62.74°, corresponding to the *hkl* values (111), (220), (311), (400), (422), (511), and (440), respectively.[40] Based on the XRD patterns, it was concluded that the prepared material exhibited a cubic structure and

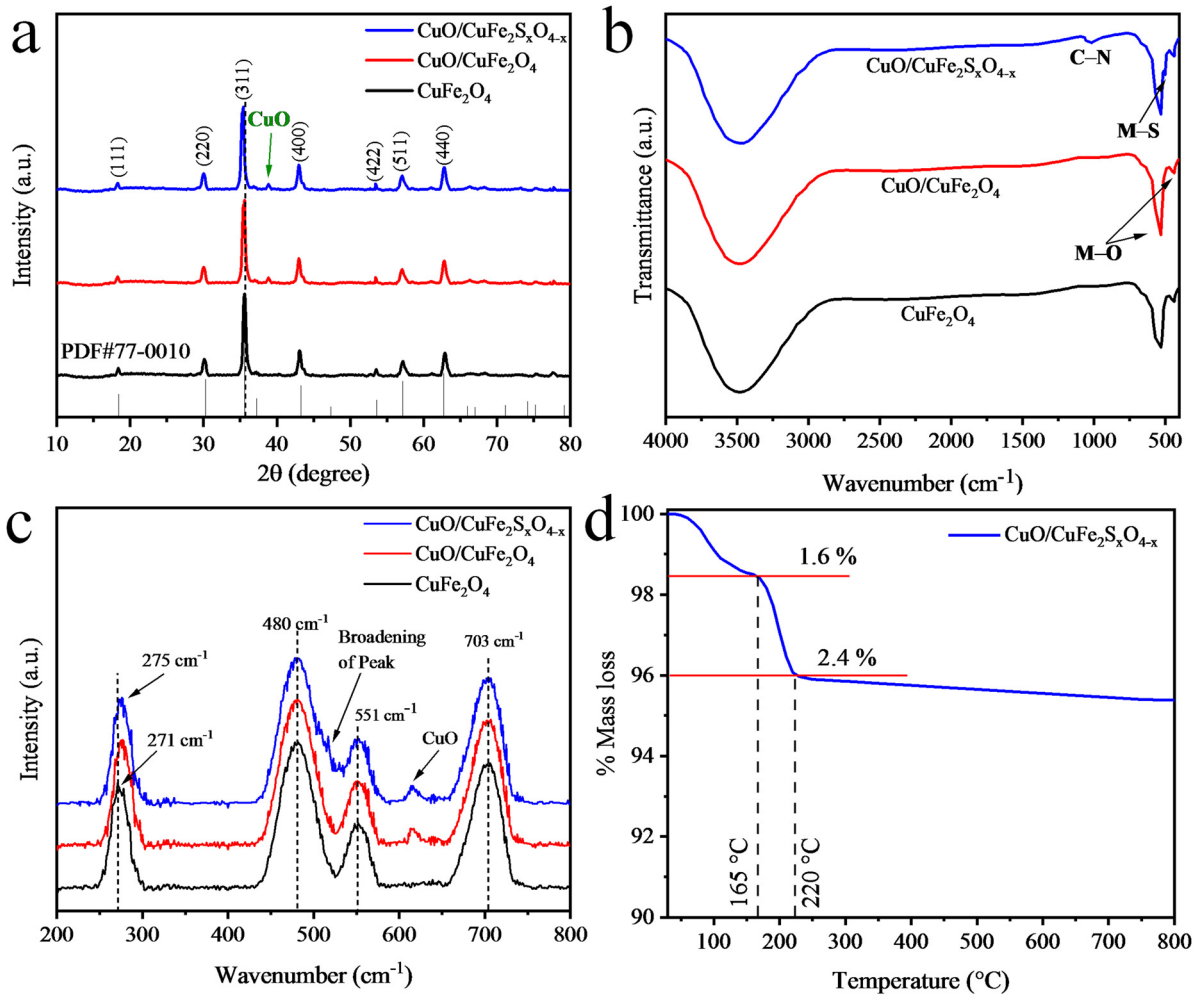

Fig. 2 (a) X-Ray diffraction patterns and (b) FTIR spectra of $CuFe_2O_4$, $CuO/CuFe_2O_4$, and $CuO/CuFe_2S_xO_{4-x}$. (c) Raman spectra and (d) TGA plot of the $CuO/CuFe_2S_xO_{4-x}$ photocatalysts.

Fe(III) and Cu(II) cations occupy the octahedral and tetrahedral places, respectively. Upon sulphur doping, the main peak (311) was significantly shifted to a lower angle, and the intensity of diffraction peaks was also decreased. These obtained results indicate that the sulphur had successfully replaced the oxygen atoms in the $CuFe_2O_4$ structure. No other crystalline phases, such as Fe_2O_3, iron sulphide, or copper sulphide, was observed, confirming the purity of the product. However, there were a few additional peaks near 65°, which could be attributed to the presence of copper oxide (CuO).[41] The sharpness of the peaks in the XRD patterns suggested the highly crystalline nature of the synthesized catalysts. The crystallite sizes of pristine $CuFe_2O_4$, $CuO/CuFe_2O_4$, and $CuO/CuFe_2S_xO_{4-x}$ were determined to be 19.88, 20.41, and 21.31 nm, respectively, using Debye–Scherrer's formula. This formula allows estimation of the average crystallite size based on the broadening of the XRD peaks.[42]

Fourier transform infrared spectroscopy (FTIR) analysis

The FTIR spectra of $CuFe_2O_4$, $CuO/CuFe_2O_4$, and $CuO/CuFe_2S_xO_{4-x}$ catalysts are depicted in Fig. 2(b). In the spectra, prominent vibrations could be observed at 531 and 437 cm^{-1}, corresponding to metal–oxygen (M–O) bond vibrations of the tetrahedral sites (where M = Fe, Cu).[43] A broad peak around 3480 cm^{-1} was also observed, associated with the bending vibration of hydroxyl groups, indicating the presence of moisture on the surface of the catalyst.[44,45] Upon sulphur doping, vibrations related to metal–sulphur bonds could be observed at approximately 500 cm^{-1}, although their intensity was lower compared to the Fe–O and Cu–O vibrational bands. The vibrations in the range of 1025–1035 cm^{-1} were attributed to the C–N stretching vibrations, likely due to the presence of thiourea.[46] The observed stretching vibrations were consistent with previous studies on sulphur-doped materials.[47] The FTIR spectra provide valuable information regarding the bonding interactions and chemical composition of the synthesized $CuFe_2O_4$ and $CuO/CuFe_2S_xO_{4-x}$ photocatalysts.

Raman analysis

Fig. 2(c) displays the Raman spectra of $CuFe_2O_4$, $CuO/CuFe_2O_4$, and $CuO/CuFe_2S_xO_{4-x}$. Group theory analysis revealed the presence of four Raman active modes, namely A_{1g}, E_g, and

two T_{2g} modes, within the range of 200–800 cm^{-1}.[48] The A_{1g} mode was observed at approximately 703 cm^{-1}, the E_g mode at around 271 cm^{-1}, and the two T_{2g} modes at approximately 480 and 551 cm^{-1}. The observed frequencies were influenced by the Fe(Cu)–O bond lengths.[49] These frequencies are sensitive to various factors, including phase transformation, lattice distortion, and cationic redistribution.[50] In the case of sulphur-doped copper ferrite, a slight shift of the E_g mode towards a lower wave number (from 271 to 275 cm^{-1}) was observed. Additionally, lattice distortion was observed between the two T_{2g} modes (broadening of peak), which could be ascribed to the presence of sulphur dopants rather than the oxygen content in the catalysts. These Raman spectroscopy findings provide insights into the structural modifications and vibrational features induced by the introduction of sulphur dopants in the $CuFe_2O_4$ structure.[51]

Thermogravimetric analysis (TGA)

Thermogravimetric analysis (TGA) was performed for the as-synthesized $CuO/CuFe_2S_xO_{4-x}$ (uncalcined catalysts) to investigate their thermal stability (Fig. 2(d)). The TGA measurements were conducted in a nitrogen (N_2) atmosphere, in the temperature range of 35–800 °C. The TGA results indicated there was a weight loss of 1.6% up to 165 °C, which was due to the removal

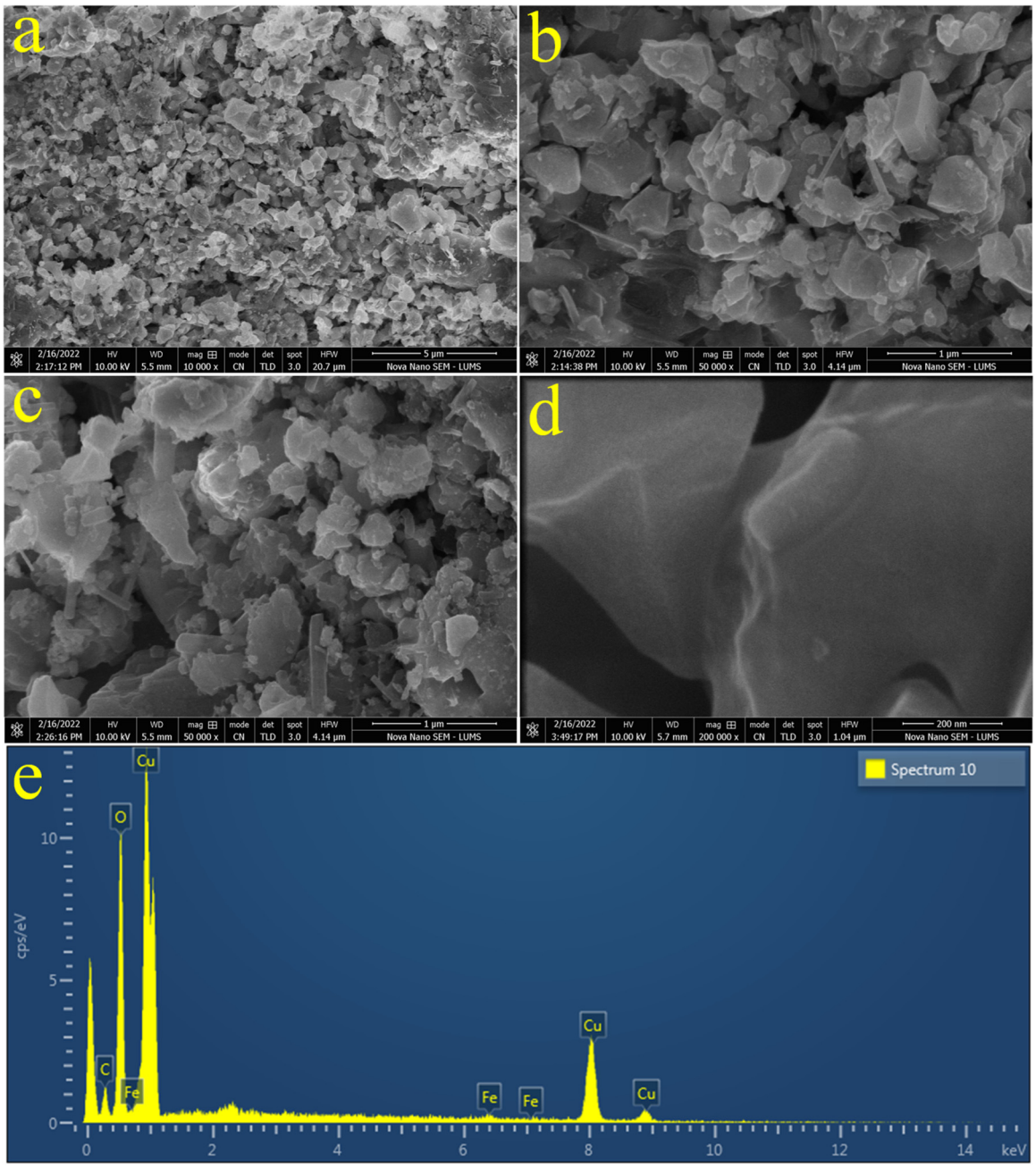

Fig. 3 (a) and (b) SEM image of $CuFe_2O_4$, (c) and (d) SEM images of $CuO/CuFe_2O_4$, and (e) EDX spectrum of $CuFe_2O_4$.

of the moisture content in the catalysts and some solvent impurities present on the catalysts' surfaces.[52] Additionally, a further weight loss of 2.4% up to 220 °C was indicated, corresponding to the decomposition of metal hydroxides. Importantly, no significant loss in weight was experienced when the temperature was enhanced to 800 °C, indicating the excellent thermal stability of the $CuO/CuFe_2S_xO_{4-x}$ nanoparticles.[53] This thermal stability is advantageous for their potential application as a photocatalyst, as it ensures that the catalysts can maintain their structural integrity and performance under elevated temperatures.[54]

Scanning electron microscopy (SEM) and EDX analyses

The morphologies of the pristine $CuFe_2O_4$ and the as-synthesized $CuO/CuFe_2S_xO_{4-x}$ photocatalysts were examined using a SEM (scanning electron microscopy) instrument equipped with a TLD sensor. The SEM results of the pristine $CuFe_2O_4$ are shown in Fig. 3(a) and (b), whereas the results for $CuO/CuFe_2O_4$ are displayed in Fig. 3(c) and (d). The results depict the agglomeration and irregular flake-like morphologies of the particles. This agglomeration could be attributed to attractive forces, such as magnetic dipole–dipole interactions.[55] On the other hand, the SEM images of the as-prepared $CuO/CuFe_2S_xO_{4-x}$ catalysts are displayed in Fig. 4(a) and (b). The SEM results clearly indicate that the introduction of sulphur doping led to a more regular morphology of the catalysts, with reduced agglomeration.[56] This suggests an increase in the sponginess of the compounds, and provides more active sites. The results demonstrate that the incorporation of sulphur increases the surface area of the catalysts, which contributes to the increased efficiency of $CuFe_2O_4$.[57] EDX analysis was also performed to determine the composition of the catalysts and the dispersion of elements in the pristine $CuFe_2O_4$ and $CuO/CuFe_2S_xO_{4-x}$ photocatalysts. The EDX results of $CuFe_2O_4$ and $CuO/CuFe_2S_xO_{4-x}$ are shown in Fig. 3(e) and 4(c), respectively. From the EDX analysis, it was confirmed that all the constituent elements of the catalyst, *i.e.* Cu, Fe, S, and O, were present. The compositions for the pristine $CuFe_2O_4$ and $CuO/CuFe_2S_xO_{4-x}$ photocatalysts are given in Tables S1 and S2 (ESI†), respectively. The EDX results confirmed the purity of the photocatalysts and the presence of sulphur dopants in the $CuFe_2O_4$ structure.[58] These analyses validated the successful incorporation of sulphur into the $CuFe_2O_4$ lattice.

AFM analysis

To investigate the surface properties of the catalysts at the nanoscale, atomic force spectroscopy (AFM) analysis was performed. AFM analysis provides important insights about the topography, surface morphology, and other physical properties. The AFM results of $CuO/CuFe_2S_xO_{4-x}$ catalysts are shown in

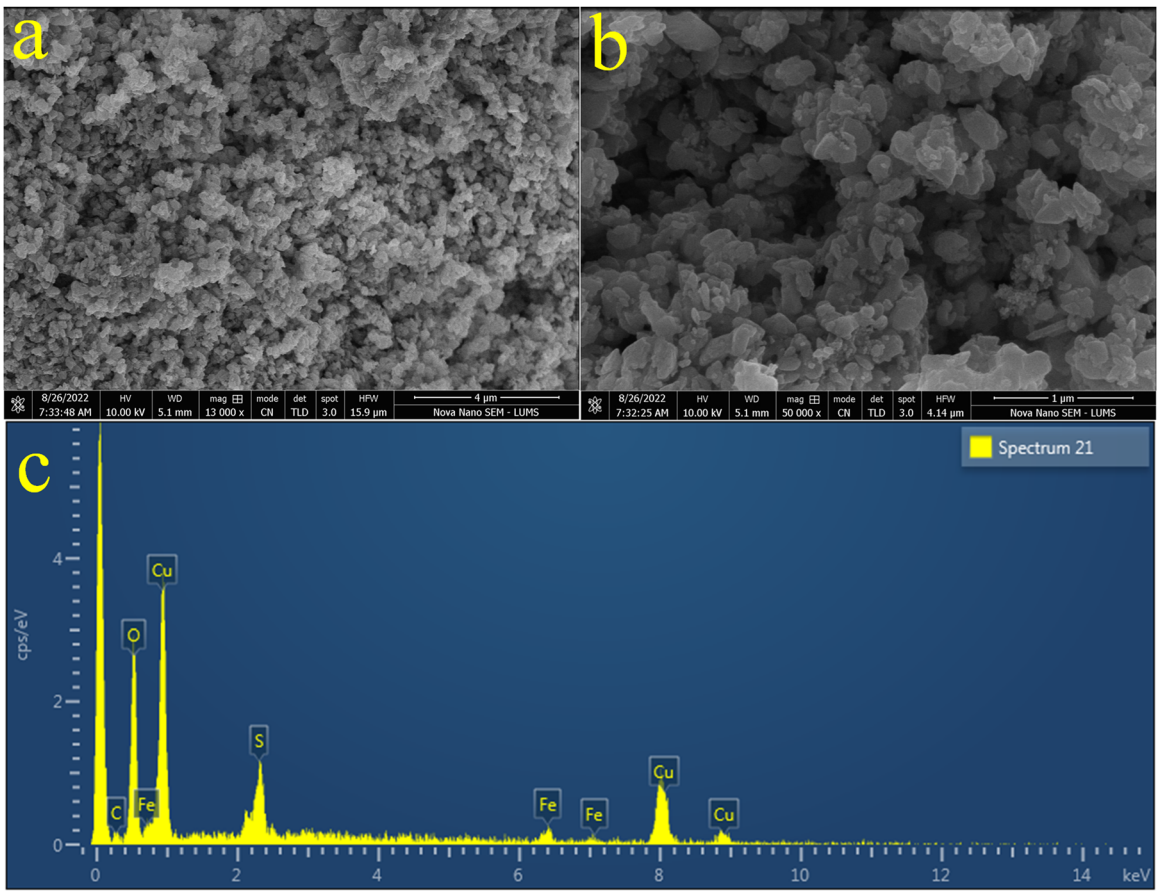

Fig. 4 (a) and (b) SEM images and (c) EDX spectrum of $CuO/CuFe_2S_xO_{4-x}$.

Fig. 5. 2D and 3D images of the catalysts are shown in Fig. 5(a), (b), (d) and (e), respectively, whereas Fig. 5(c) shows a histogram representing the thickness of the photocatalyst. The maximum surface thickness of the catalyst was 3.82 nm, whereas the scan area for measurement of the catalysts was 2.83 × 2.49 μm, respectively.

Ultraviolet-visible-diffuse reflectance spectroscopy analysis

The optical properties of the pristine $CuFe_2O_4$, $CuFe_2S_xO_{4-x}$, $CuO/CuFe_2O_4$, and $CuO/CuFe_2S_xO_{4-x}$ were examined using UV-Vis-Diffuse reflectance spectroscopy (UV-Vis-DRS). This technique is utilized for powdered samples due to its ability to minimize scattering effects, unlike absorption spectroscopy conducted on liquids.[59] In Fig. 6(a), an absorption edge could be observed, indicating an Urbach-like absorption tail in the visible region.[60] Pristine $CuFe_2O_4$ displayed a maximum absorption at approximately 688 nm, corresponding to an optical bandgap (E_g) of 1.77 eV.[61] The optical band gap represents the minimum energy required to promote an electron from the valence band to the conduction band. The S-doping resulted in a reduction of the bandgap energy by 0.3 eV. Conversely, loading CuO over $CuFe_2O_4$ caused a blue-shift in the absorbance spectrum (Fig. 6(b)). Upon S-doping, a red-shift in the visible-light absorption was observed; with an absorbance edge at 696 nm (E_g = 1.82 eV). This red-shift suggests an enhanced visible-light response, indicating that the sulphur doping contributed to higher photocatalytic activities. The increased visible-light absorption allows the catalyst to harvest a broader range of wavelengths and utilize more photons for the photocatalytic process. Overall, the UV-Vis-DRS results provide valuable insights into the optical properties of pristine $CuFe_2O_4$ and $CuO/CuFe_2S_xO_{4-x}$, demonstrating the influence of sulphur doping on their visible-light absorption and potential photocatalytic performance. Relevant band gaps of $CuFe_2O_4$, $CuO/CuFe_2O_4$, and $CuO/CuFe_2S_xO_{4-x}$ are shown in Fig. 6(b).

Photoluminescence analysis

PL analysis of the synthesized $CuFe_2O_4$, $CuO/CuFe_2O_4$, and $CuO/CuFe_2S_xO_{4-x}$ photocatalysts was performed as it can provide important insights into the photogenerated charges (e^-/h^+) recombination and their transfer to the active sites.[62] In the $CuFe_2O_4$ results, three broad peaks were observed at wavelengths of 422, 467, and 554 nm, see Fig. 6(c). The blue emission due to the presence of some defects in the catalysts appeared at 468 nm. Similarly, the presence of defects (caused by oxygen vacancies) could be observed by the peak at 553 nm. The presence of CuO reduces the PL intensity, which indicated the influences of cocatalyst on the charge separation. In the case of $CuO/CuFe_2S_xO_{4-x}$, the emission intensity was further reduced, indicating the incorporation of sulphur also influenced the photoluminescence properties. This decrease in PL intensity suggests a low charge recombination and more transfer of electrons to the active sites. In $CuO/CuFe_2S_xO_{4-x}$ the PL emissions caused by oxygen vacancies were marginally shifted to 549 nm, indicating the presence of new electronic levels. This shift also implied that the recombination of charge carriers (e^-/h^+) was significantly reduced in the $CuO/CuFe_2S_xO_{4-x}$

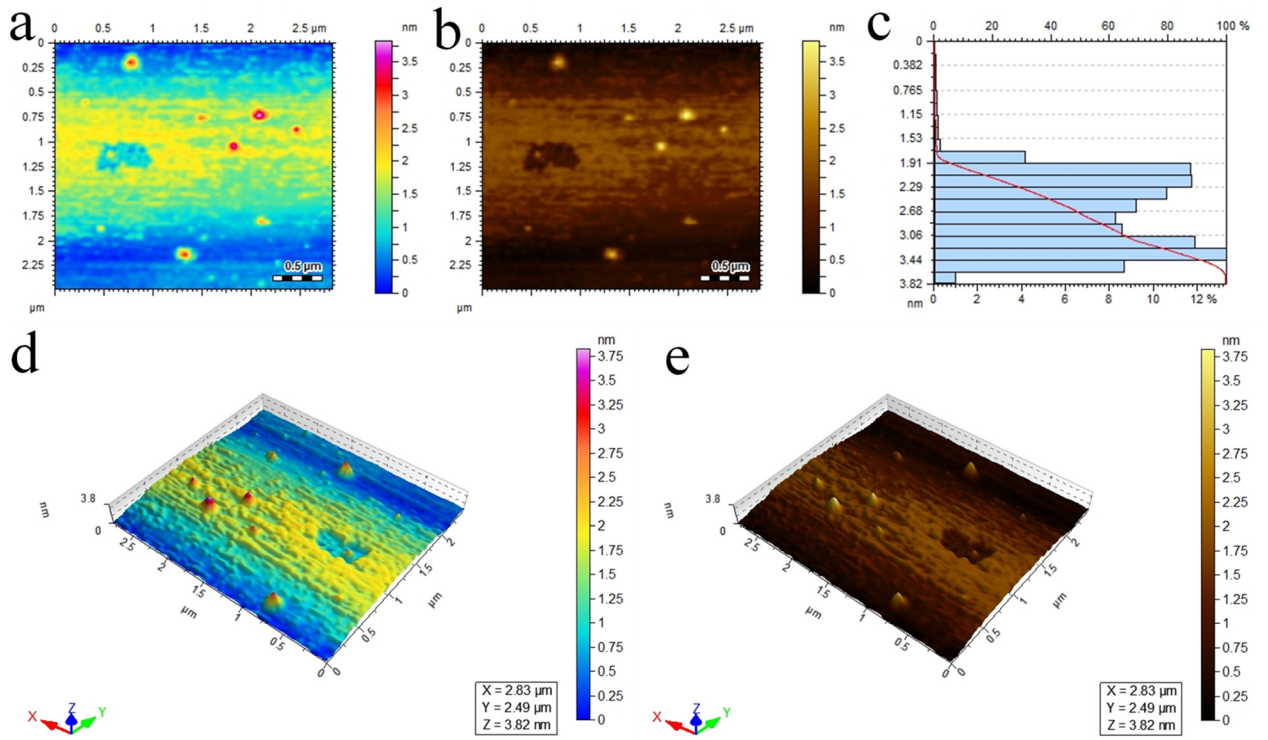

Fig. 5 Atomic force spectroscopy analysis. (a) and (b) 2D images, (c) height of the catalysts, (d) and (e) 3D images of the $CuO/CuFe_2S_xO_{4-x}$ catalysts.

catalysts, leading to their improved photocatalytic performance. The introduction of sulphur doping creates additional mid-gap states within the band structure of the catalysts. These states act as a charge-separating centres due to the presence of doped sulphur atoms.[26] It was evident that $CuO/CuFe_2S_xO_{4-x}$ exhibited efficient charge-carrier separation and could show remarkable performance for photocatalytic hydrogen generation.

BET analysis

The surface areas of the catalysts were determined by Brunauer–Emmett–Teller (BET) analysis. Usually, catalysts with a large surface area exhibit a high efficiency for photoreactions. The surface area of pristine $CuFe_2O_4$ was 44.52 $m^2\ g^{-1}$ as calculated using the Brunauer–Emmett–Teller theorem.[63] When CuO was loaded on $CuFe_2O_4$, the surface area increased to 48.68 $m^2\ g^{-1}$, as depicted by the N_2 adsorption and desorption curves demonstrated in Fig. 6(d). Furthermore, the S-doped $CuO/CuFe_2O_4$ exhibited a higher surface area of 110.4 $m^2\ g^{-1}$.

XPS analysis

XPS analysis was next performed to investigate the oxidation state and chemical composition of the elements present in the $CuO/CuFe_2S_xO_{4-x}$ photocatalysts.[64] The XPS spectrum of $CuO/CuFe_2S_xO_{4-x}$ indicated the presence of all the essential elements (*i.e.* S, Cu, Fe, and O). The XPS results of Cu are presented in Fig. 7(a), displaying two major peaks for Cu at 934.5 and 954.7 eV corresponding to $2p_{3/2}$ and $2p_{1/2}$, respectively, and with the binding energy of XPS indicating that Cu was present in the +2 oxidation state. Fig. 7(b) presents the XPS spectrum of Fe 2p, in which two major peaks could be observed at 711 and 723.2 eV, ascribed to the $2p_{3/2}$ and $2p_{1/2}$, respectively. These peaks indicate that Fe was present in the +3 oxidation state, similar to the reported literature. Some iron atoms also existed in the +2 oxidation state due to the formation of FeO in $CuFe_2O_4$, whose peak appeared at 710.11 eV. Doped atoms of sulphur were also investigated and major peaks of sulphur $2p_{3/2}$ and $2p_{1/2}$ were observed at 160.99 and 162.21 eV, see Fig. 7(c). The XPS spectrum displayed the O 1s peaks at 529.02, 530.98, and 532.08 eV (Fig. 7(d)). The confirmation of three distinct oxygen binding energies through XPS analysis showed the presence of three different oxygen environments, elucidating the coexistence of CuO contents within our synthesized $CuO/CuFe_2S_xO_{4-x}$ photocatalysts.[65,66]

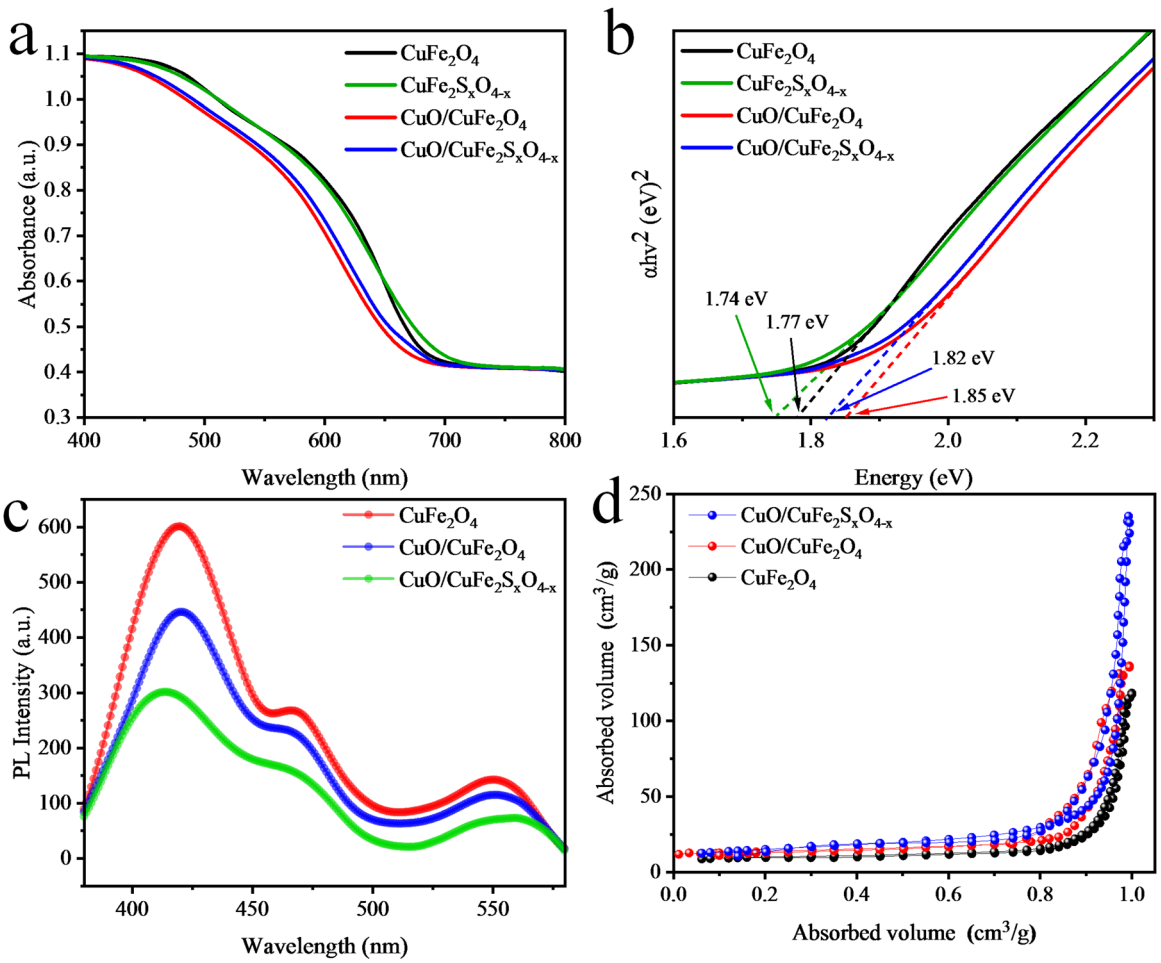

Fig. 6 (a) Ultraviolet-visible-diffuse reflectance spectroscopy plots, (b) Tauc plots, (c) PL analysis plots, and (d) BET N_2 adsorption–desorption isotherms measured at 77 K.

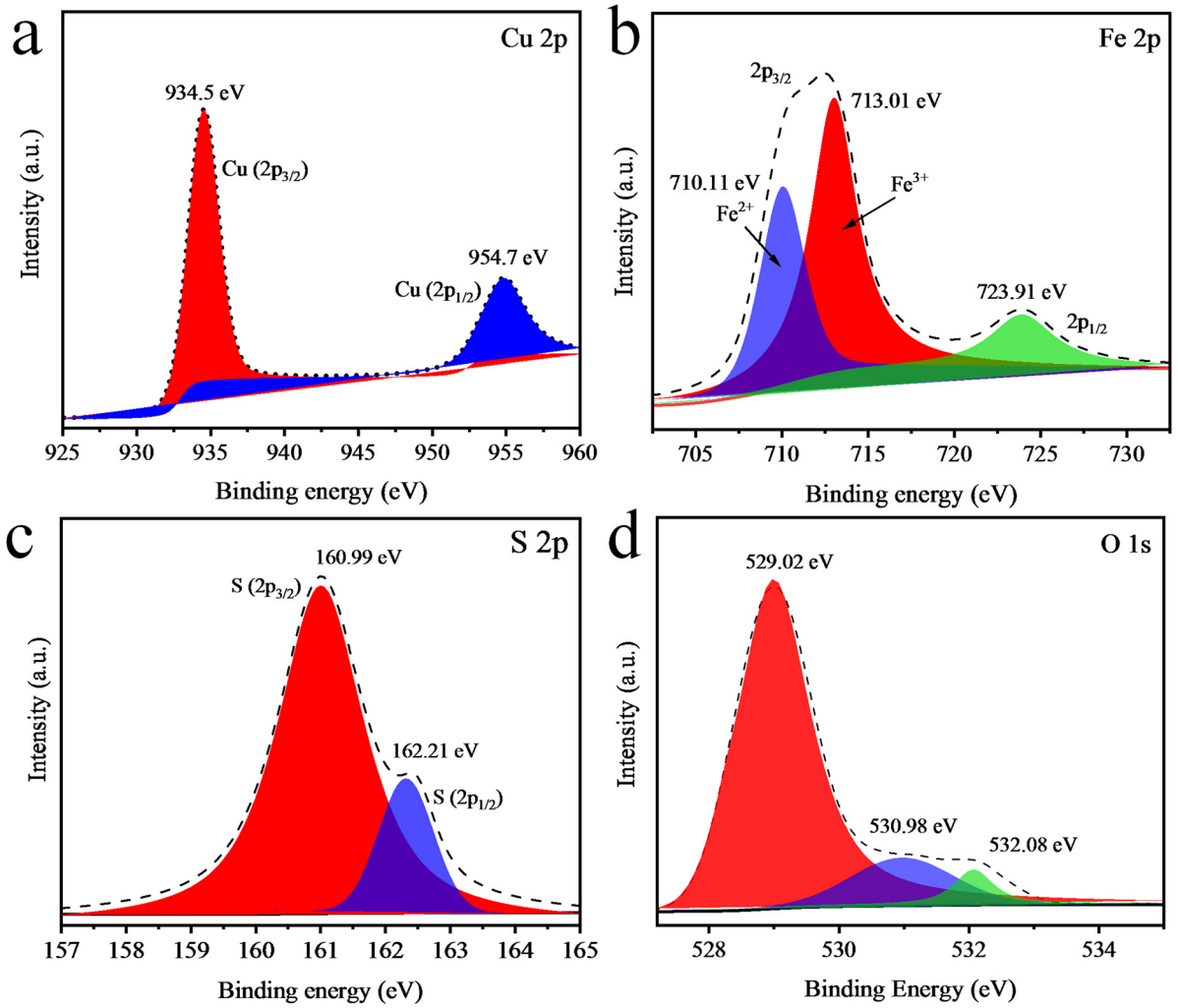

Fig. 7 XPS analysis of $CuO/CuFe_2S_xO_{4-x}$: (a) Cu 2p, (b) Fe 2p, (c) S 2p, and (d) O 1s.

VSM analysis

The magnetic properties of the catalysts were investigated through vibrating-sample magnetometry (VSM) analysis by studying their hysteresis loops (Fig. 8(a)). These magnetic measurements offer valuable insights in to the saturated magnetic intensity (M_s), residual magnetic intensity (M_r), coercivity (H_c), and squareness ratio. At 300 K, the $CuO/CuFe_2S_xO_{4-x}$ photocatalyst showed an M_r value of 7.04 emu g^{-1} and M_s value of 31.6 emu g^{-1}, as determined from the VSM plots.[66,67] Table S3 (ESI†) shows the magnetic parameters (M_s, M_r, H_c, and squareness ratio) of the as-synthesized catalysts.

EPR analysis

The electronic characteristics of the as-synthesised catalysts at room-temperature were determined by electron paramagnetic resonance (EPR) (Fig. 8(b)). The as-synthesised catalysts displayed EPR signals with a *g*-factor of 2.00, attributed to the presence of unpaired electrons within their structures. $CuO/CuFe_2SO_{4-x}$ demonstrated an increased concentration of unpaired electrons compared to $CuO/CuFe_2O_4$ and $CuFe_2O_4$.[68] This increased concentration was attributed to structural alterations induced by the presence of CuO and S-doping in $CuFe_2O_4$. The electronic distribution within the $CuO/CuFe_2SO_{4-x}$ structure positively influences the separation and mobility of photoinduced carriers.[69]

Electrochemical studies

Electron impedance spectroscopy (EIS) and photocurrent analyses were performed to assess the electrochemical performance of the catalysts. Photocurrent measurements were taken for $CuFe_2O_4$, $CuFeS_xO_{4-x}$, $CuO/CuFe_2O_4$, and $CuO/CuFeS_xO_{4-x}$ during on/off light cycles. The results revealed that $CuFe_2O_4$ exhibited low charge-transfer and -separation abilities compared to the $CuO/CuFeS_xO_{4-x}$ catalysts. Whereas, the results presented in Fig. 8(a) revealed that sulphur dopants and CuO significantly improved the charge-transfer and -separation abilities.

EIS analyses were conducted to examine the charge-transfer resistance. The results are shown in Fig. 8(b) and revealed that the $CuO/CuFeS_xO_{4-x}$ catalysts exhibited the smallest arc radius compared to the other catalysts in the series. These results

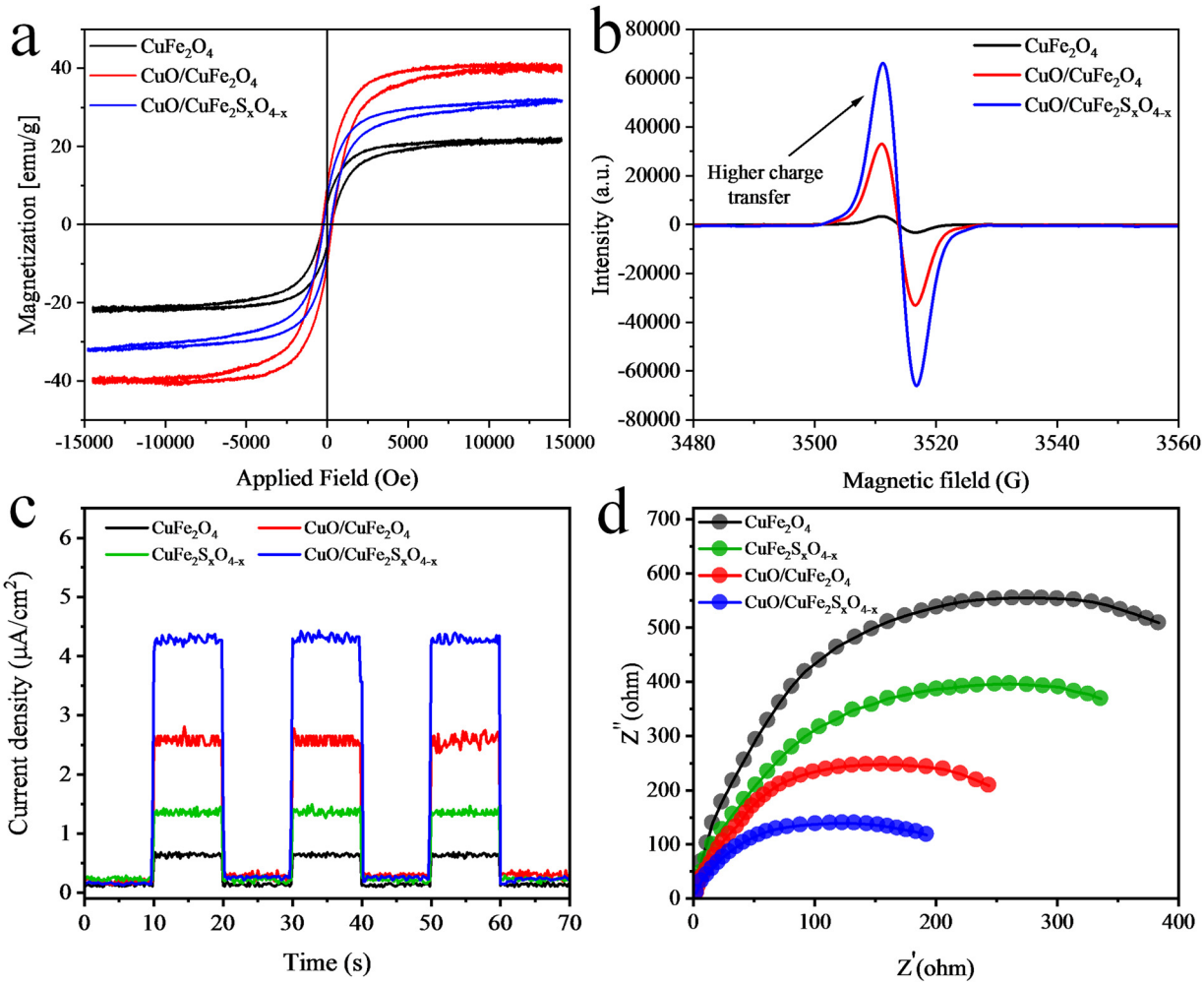

Fig. 8 (a) VSM hysteresis loops, (b) EPR results, (c) photocurrent, and (d) EIS results for the catalysts.

suggest that S-doping and the presence of CuO can effectively reduce the charge-transfer resistance and enhance charge transfer for photocatalytic H_2-generation reactions.

Photocatalytic activities

Fig. 9(a) and (b) present the H_2-evolution activities of the as-synthesized photocatalysts in the presence of visible light and a sacrificial reagent. For each photocatalytic experiment, the total time was fixed and optimized for 6 h to test the activity of the catalyst. In the absence of light and a photocatalyst, no hydrogen was produced from the water in the photoreactor. In the first experiment, pristine $CuFe_2O_4$ was employed and it produced a meagre amount of hydrogen, and these results suggest that bare $CuFe_2O_4$ is not a suitable photocatalyst for H_2 production. In the second experiment, the S-doping slightly increased the H_2-evolution rate to 2.24 mmol g^{-1} h^{-1}. Whereas, $CuO/CuFe_2O_4$ produced 3.85 mmol g^{-1} h^{-1} of H_2 compared to the pristine $CuFe_2O_4$, which produced only 1.48 mmol g^{-1} h^{-1}.[70] Furthermore, the combined effect of S-doping and the CuO content in $CuO/CuFe_2S_xO_{4-x}$ boosted the photocatalytic hydrogen evolution activities to produce 7.45 mmol g^{-1} h^{-1} of H_2 (see Fig. 9(a) and (b) and Table 1). The increase in the activity of the photocatalyst for hydrogen production could be ascribed to the CuO content and S-doping in the $CuFe_2O_4$. The CuO content enhances the oxidation potential of semiconductors and S-doping prevents the electron–hole charge recombination, due to which the activity of the as-synthesized $CuO/CuFe_2S_xO_{4-x}$ photocatalyst was increased.[71] $CuO/CuFe_2S_xO_{4-x}$ exhibited higher activities in the presence of sacrificial reagents. These sacrificial reagents consume the holes created in the valence band of the semiconductor and promote the transfer of electrons for hydrogen production. It is important to distinguish whether the H_2 is coming from water or the dehydrogenation of ethanol; for this purpose, photocatalytic H_2 evolution in the presence of S^{2-}/SO_3^{2-} mixtures was conducted, with the detailed presented in the ESI,† see Fig. S1. The reaction mechanism is depicted in eqn (S1)–(S6) (ESI†). These results aligned and were consistent with the findings observed in the presence of ethanol. The results recommend that water was the main source of H_2 evolution, while the ethanol and S^{2-}/SO_3^{2-} only acted as hole scavengers.

The efficiency of the photocatalyst was also compared with other reported ferrites and the as-prepared $CuO/CuFe_2S_xO_{4-x}$

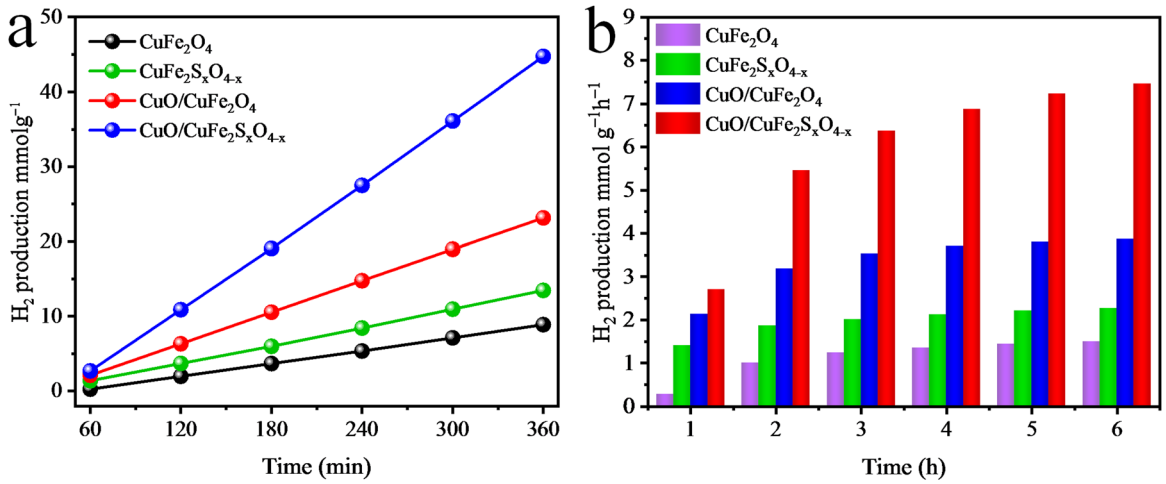

Fig. 9 H_2 evolution activities of the as-synthesised catalysts in (a) mmol g^{-1} and (b) mmol g^{-1} h^{-1}.

Table 1 Comparison of the H_2 evolution and AQY of the as-synthesized photocatalysts

	H_2 evolution		
Photocatalysts ⁑	mmol g^{-1} h^{-1}	mmol g^{-1}	AQY (%)
$CuFe_2O_4$	1.48	8.88	0.48
$CuFe_2S_xO_{4-x}$	2.24	13.48	0.73
$CuO/CuFe_2O_4$	3.85	23.14	1.26
$CuO/CuFe_2S_xO_{4-x}$	7.45	44.73	2.45

Where ⁑ = 10 mg amount of catalysts used for the experiment in a 30 mL reaction mixture (5% ethanol) in the reactor having a volume of 150 mL and reaction time of 6 h.

catalyst, see Table 2. This comparison allows the evaluation and comparison of the effectiveness of different catalysts for the evolution of hydrogen. Table 2 provides valuable insights into the performance of different catalysts for hydrogen production. It allows researchers to assess and compare the efficiency of various catalysts in terms of their effectiveness for hydrogen production. This information is important for selecting suitable catalysts for effective photocatalytic hydrogen production.

Recyclability

The above results clearly demonstrate the higher photocatalytic efficiency of $CuO/CuFe_2S_xO_{4-x}$ nanostructures compared to pristine $CuFe_2O_4$. The introduction of sulphur atoms in the $CuFe_2O_4$ structure creates additional active sites, improving interactions with the water molecules.[75] Furthermore, the electronic structure of the catalysts was improved, leading to a variation in the energy level and bandgap due to the doping of sulphur atoms.[76] These modifications enhance the charge separation, resulting in efficient hydrogen generation. Additionally, the $CuO/CuFe_2S_xO_{4-x}$ photocatalysts possess good magnetic properties; whereby an external magnet could be used for the easy separation of the catalyst from the reaction mixture. This method is simple, speedy, and more effective than the conventional methods (*i.e.* centrifugation and filtration). The use of $CuO/CuFe_2S_xO_{4-x}$ photocatalysts not only enhances the photocatalytic efficiency but also removes the danger of pollution and ensures their full utilization over extended periods. Next, to evaluate the recyclability of $CuO/CuFe_2S_xO_{4-x}$, tests were conducted after thorough washing and drying of the catalyst. The recyclability results for hydrogen generation using $CuO/CuFe_2S_xO_{4-x}$ are presented in the Fig. S2 (ESI†). After 6 cycles, a slight decrease in the catalyst efficiency was observed, which could be attributed to the loss of a small amount of catalyst during the recovery process. Despite this slight decrease, the $CuO/CuFe_2S_xO_{4-x}$ photocatalysts demonstrated promising recyclability, indicating their potential for repeated use for photocatalytic applications.[77]

Mechanism

Catalysts with a suitable band gap can split water for efficient hydrogen evolution. During photocatalytic reactions, oxidation and reduction reactions take place simultaneously.[78] In the case of water-oxidation reactions, the oxidation potential of the photocatalyst should be more positive than 1.23 eV. In comparison, the oxidation of ethanol needs a potential of 0.084 eV (*vs.* NHE).[79] For the reduction reaction, the reduction potential should be more negative than the reduction potential of

Table 2 Comparison of photocatalytic H_2 evolution rates achieved by $CuFe_2O_4$ based catalysts reported in the literature

Catalysts	Light source	Catalyst amount	Sacrificial reagent	H_2 production	Ref.
$CuO/CuFe_2S_xO_{4-x}$	Sunlight	10 mg	5% ethanol	7.45 mmol g^{-1} h^{-1}	This study
$CuFe_2O_4$	Visible light	10 mg	Oxalic acid	1.72 mmol g^{-1} h^{-1}	72
$CuFe_2O_4$/MnO		7.5 mg	Na_2SO_3	0.50 mmol g^{-1} h^{-1}	73
$CuFe_2O_4$/rGO		5 mg	None	622 mL min^{-1} g^{-1}	74

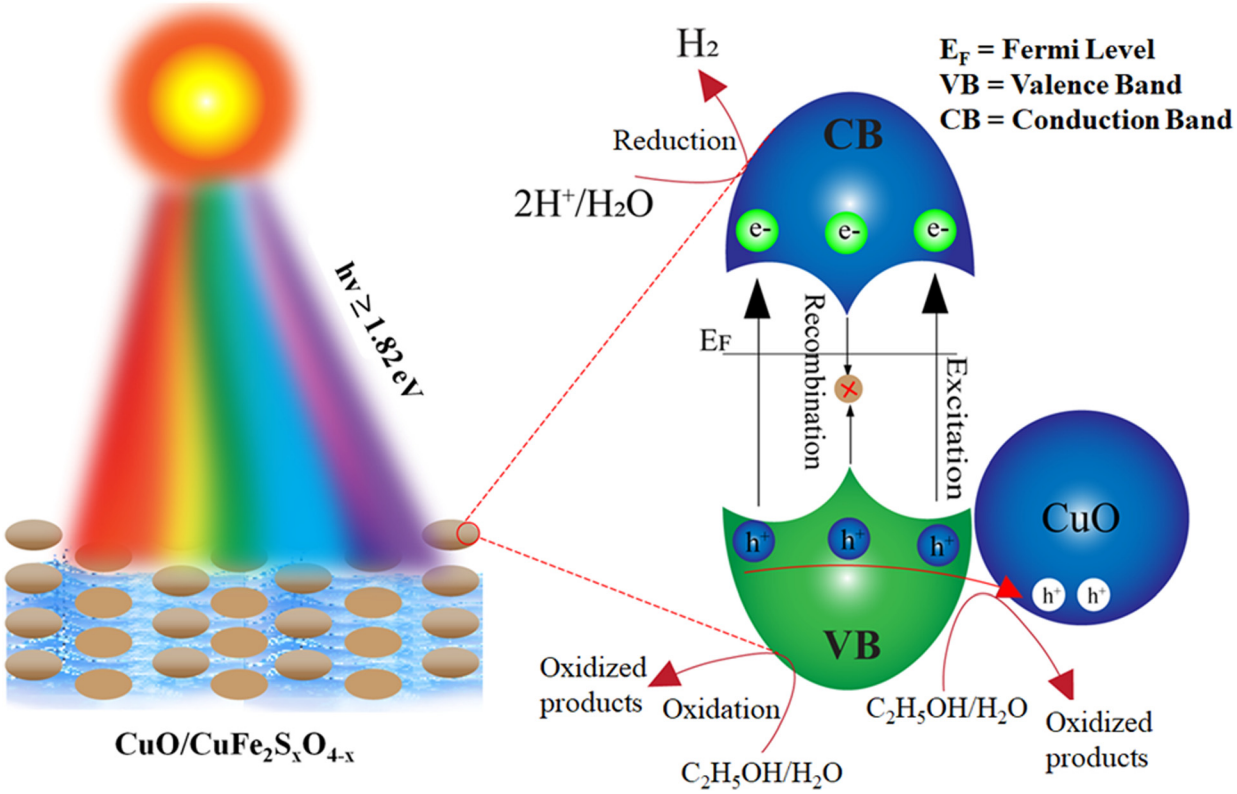

Fig. 10 Photocatalytic mechanism of the water-splitting reaction over $CuO/CuFe_2S_xO_{4-x}$ photocatalysts.

hydrogen.[80–82] The oxidation potential of $CuFe_2O_4$ is 1.03 eV, which is not sufficient to split the water efficiently. The CuO content present in $CuFe_2O_4$ plays an important role here. CuO has a high oxidation potential greater than the 1.23 eV and has the ability to carry out the oxidation reaction. Furthermore, sulphur atoms were doped to transfer the electrons towards active sites for hydrogen generation, whereby the dopant atoms also suppress the recombination of charges (e^-/h^+). Moreover, a sacrificial reagent (C_2H_5OH) was also used to consume the holes generated in the valence band, whereby the recombination of charges is reduced. These holes convert the organic reagents into oxidized products (water and CO_2).

When light falls on the photocatalytic reaction mixture, the catalyst absorbs the light and generates charges (e^-/h^+).[83] In the absence of light, no photoreaction occurred. Electrons migrate towards the conduction band of the semiconductor, where these electrons are utilized for the reduction reaction and result in the generation of hydrogen,[84] as shown in Fig. 10 and Scheme 1. As the catalysts absorbs more light, then the migration of electrons towards the conduction band increases and produces more hydrogen.[85] In the valence band, sacrificial reagents quench the holes and in the oxidation process they are converted into oxidized products.

$CuO/CuFe_2S_xO_{4-x} + hv \longrightarrow$ (VB) h^+ + (CB) e^- (i)

Photocatalyst + $H_2O \longrightarrow H^+ + OH^-$ $\Delta G^o = 237.2$ kJ mol^{-1} (ii)

$2e^- + 2H^+ \longrightarrow H_2$ $E_{CB} = 0.0$ eV (iii)

$2h^+ + C_2H_5OH \longrightarrow$ Oxidized products $E_{VB} = 0.084$ eV (iv)

Photocatalyst + $C_2H_5OH \longrightarrow H_2$ + Oxidized products (v)

Scheme 1 Hydrogen generation mechanism over $CuO/CuFe_2S_xO_{4-x}$ with ethanol as a sacrificial agent.

Conclusion

The synthesis and characterization of $CuFe_2O_4$, $CuO/CuFe_2O_4$, and $CuO/CuFe_2S_xO_{4-x}$ photocatalysts were successfully conducted in this study. Various analytical techniques, such as XRD, Raman, FT-IR, SEM, EDX, and TGA, were employed to investigate the structural properties, compositions, and stability of the synthesized catalysts. The results confirmed the hydrothermal synthesis of crystalline $CuFe_2O_4$ and the incorporation of sulphur into the lattices. The structural analyses revealed that the introduction of sulphur doping induced lattice strain and caused the replacement of oxygen with sulphur anions within the lattice structures of $CuFe_2O_4$. SEM analysis further supported the idea that sulphur doping reduces the chances of agglomeration and enhanced the availability of active sites for hydrogen evolution. EDX analysis has provided the direct evidence of sulphur in synthesized $CuO/CuFe_2S_xO_{4-x}$ photocatalysts, confirming the successful S-doping into $CuFe_2O_4$ structures. The TGA results indicated the thermal stability of S-$CuFe_2O_4$ photocatalysts for practical applications. PL studies assured that sulphur acted as an electron-trapping centre, effectively suppressing charge recombination

during the photocatalytic reaction. The low charge recombination indicated that sulphur doping contributed to improved electron–hole separation and enhanced the photocatalytic performance of $CuO/CuFe_2S_xO_{4-x}$. The magnetic and electronic properties of catalysts were investigated *via* VSM and EPR techniques. The hydrogen-evolution activities of $CuFe_2O_4$ and $CuO/CuFe_2S_xO_{4-x}$ were calibrated by the internal calibration curve with GC-TCD system. Upon comparison of the photocatalytic activities, it could be concluded that $CuO/CuFe_2S_xO_{4-x}$ exhibited superior performances for H_2-generation reactions. The successful synthesis, characterization, and evaluation of $CuO/CuFe_2S_xO_{4-x}$ highlight its potential for various applications in photocatalysis and provide valuable insights for further research in this field.

Data availability

The data and necessary protocols of this study have been included as part of the ESI.†

Conflicts of interest

There are no conflicts to declare.

Acknowledgements

This research work was funded by HEC of Pakistan with grant number 377/IPFP-II/Batch-I/SRGP/NAHE/HEC/2022/27 and ASIP/R&D/HEC/2023/5/22696/124. Catalysts preparation and hydrogen performances were done at Inorganic Materials Laboratory 52S, Institute of Chemistry, The Islamia University of Bahawalpur Pakistan.

References

1 K. H. H. Aziz, F. S. Mustafa, K. M. Omer, S. Hama, R. F. Hamarawf and K. O. Rahman, *RSC Adv.*, 2023, **13**, 17595–17610.
2 J. Rieuwerts, *The elements of environmental pollution*, Routledge, 2017.
3 A. Demirbas, *Energy Sources*, 2004, **26**, 225–236.
4 F. M. Alptekin and M. S. Celiktas, *ACS Omega*, 2022, **7**, 24918–24941.
5 S. Chen, T. Takata and K. Domen, *Nat. Rev. Mater.*, 2017, **2**, 1–17.
6 A. Garg, T. Singhania, A. Singh, S. Sharma, S. Rani, A. Neogy, S. R. Yadav, V. K. Sangal and N. Garg, *Sci. Rep.*, 2019, **9**, 765.
7 C. Jiang, S. J. Moniz, A. Wang, T. Zhang and J. Tang, *Chem. Soc. Rev.*, 2017, **46**, 4645–4660.
8 X. Xu, C. Randorn, P. Efstathiou and J. T. Irvine, *Nat. Mater.*, 2012, **11**, 595–598.
9 S. Huang, M. Wang and X. Jiang, *Chem. Soc. Rev.*, 2022, **51**, 8351–8377.
10 Z. Zhang, G. Yi, P. Li, X. Zhang, H. Fan, Y. Zhang, X. Wang and C. Zhang, *Nanoscale*, 2020, **12**, 13899–13906.
11 F. Ahmad, K. Rafiq, T. Najam, E. Hussain, M. Sohail, M. Z. Abid, A. Mahmood, M. S. Javed and S. S. A. Shah, *Int. J. Hydrogen Energy*, 2023, **48**, 35075–35111.
12 A. Bumajdad and M. Madkour, *Phys. Chem. Chem. Phys.*, 2014, **16**, 7146–7158.
13 L. Zhou, H. Zhang, H. Sun, S. Liu, M. O. Tade, S. Wang and W. Jin, *Catal. Sci. Technol.*, 2016, **6**, 7002–7023.
14 M. Z. Abid, K. Rafiq, A. Rauf, R. H. Althomali and E. Hussain, *Mater. Adv.*, 2024, **5**, 2238–2252.
15 M. Z. Abid, K. Rafiq, A. Aslam, R. Jin and E. Hussain, *J. Mater. Chem. A*, 2024, **12**, 7351–7395.
16 Y. Negishi, M. Mizuno, M. Hirayama, M. Omatoi, T. Takayama, A. Iwase and A. Kudo, *Nanoscale*, 2013, **5**, 7188–7192.
17 M. Jalil, K. Rafiq, M. Z. Abid, M. Rafay, A. Rauf, R. Jin and E. Hussain, *Catal. Sci. Technol.*, 2024, **14**, 850–862.
18 R. Sharma, S. Bansal and S. Singhal, *RSC Adv.*, 2015, **5**, 6006–6018.
19 R. K. Sharma, P. Yadav, M. Yadav, R. Gupta, P. Rana, A. Srivastava, R. Zbořil, R. S. Varma, M. Antonietti and M. B. Gawande, *Mater. Horiz.*, 2020, **7**, 411–454.
20 K. Harish, H. B. Naik and R. Viswanath, *Catal. Sci. Technol.*, 2012, **2**, 1033–1039.
21 Y. Wang, S. Zhong, Z. Niu, Y. Dai and J. Li, *Chem. Commun.*, 2023, **59**, 10883–10911.
22 X. Zhang, T. Wang, Z. Zhang, H. Liu, L. Li, A. Wang, J. Ouyang, T. Xie, L. Zhang and J. Xue, *Mater. Today*, 2023, **68**, 177–203.
23 A. Rayar, C. Naveen, H. Onkarappa, V. S. Betageri and G. Prasanna, *Synth. Met.*, 2023, **295**, 117338.
24 S. Mishra and R. Acharya, *J. Alloys Compd.*, 2023, 170576.
25 V. Patel, A. Baskar, S. Tiburcius, B. Morrison, B. Mod, P. S. Tanwar, P. Kumar, A. Karakoti, G. Singh and A. Vinu, *Adv. Sens. Res.*, 2023, 2300024.
26 A. Aslam, M. Z. Abid, K. Rafiq, A. Rauf and E. Hussain, *Sci. Rep.*, 2023, **13**, 6306.
27 D. A. Peixoto, S. C. Silva, P. H. Borges, R. C. Lima and E. Nossol, *J. Mater. Sci.*, 2023, **58**, 2993–3024.
28 M. Shandilya, R. Rai and J. Singh, *Adv. Appl. Ceram.*, 2016, **115**, 354–376.
29 H. Boulahbel, M. Benamira, F. Bouremmad, N. Ahmia, S. Kiamouche, H. Lahmar, A. Souici and M. Trari, *Inorg. Chem. Commun.*, 2023, **154**, 110921.
30 H. Naseer and T. Iqbal, *Biomass Convers. Biorefin.*, 2023, 1–17.
31 Y. Wudil, U. Ahmad, M. Gondal, M. A. Al-Osta, A. Almohammedi, R. Said, F. Hrahsheh, K. Haruna and J. Mohammed, *Arabian J. Chem.*, 2023, 104542.
32 T. Zhang, C. Hu, J. Wu, B. Shen, S. Peng, Y. Qi, M. Tao, X. Mao, Y. Tao and Y. Wang, *Sep. Purif. Technol.*, 2023, 124352.
33 S. Bera, S. Ghosh, T. Maiyalagan and R. N. Basu, *ACS Appl. Energy Mater.*, 2022, **5**, 3821–3833.
34 A. A. Dubale, A. G. Tamirat, H.-M. Chen, T. A. Berhe, C.-J. Pan, W.-N. Su and B.-J. Hwang, *J. Mater. Chem. A*, 2016, **4**, 2205–2216.
35 Y. Wang, M. Zhou, Y. He, Z. Zhou and Z. Sun, *J. Alloys Compd.*, 2020, **813**, 152184.

36 A. Ismael, A. El-Shazly, S. Gaber, M. Rashad, A. Kamel and S. Hassan, *RSC Adv.*, 2020, **10**, 34806–34814.
37 C. Karunakaran, P. Vinayagamoorthy and J. Jayabharathi, *RSC Adv.*, 2016, **6**, 1782–1791.
38 E. Hussain, I. Majeed, M. A. Nadeem, A. Badshah, Y. Chen, M. A. Nadeem and R. Jin, *J. Phys. Chem. C*, 2016, **120**, 17205–17213.
39 M. Z. Abid, K. Rafiq, A. Rauf, R. H. Althomali, R. Jin and E. Hussain, *Renewable Energy*, 2024, 120223.
40 J. Zheng, Z. Lin, W. Liu, L. Wang, S. Zhao, H. Yang and L. Zhang, *J. Mater. Chem. B*, 2014, **2**, 6207–6214.
41 S. Z. Alsheheri and A. A. Ismail, *J. Taiwan Inst. Chem. Eng.*, 2023, **149**, 105015.
42 P. N. Dave, R. Thakkar, R. Sirach and S. Chaturvedi, *Mater. Adv.*, 2022, **3**, 5019–5026.
43 H. Zhang, S. Gao, N. Shang, C. Wang and Z. Wang, *RSC Adv.*, 2014, **4**, 31328–31332.
44 M. V. Vener and J. Sauer, *Phys. Chem. Chem. Phys.*, 2005, **7**, 258–263.
45 N. Wajid, K. Rafiq, M. Z. Abid, A. Ilyas, T. Najam, A. Rauf and E. Hussain, *Mater. Chem. Phys.*, 2023, **306**, 128062.
46 Z. Mirzaeifard, Z. Shariatinia, M. Jourshabani and S. M. Rezaei Darvishi, *Ind. Eng. Chem. Res.*, 2020, **59**, 15894–15911.
47 C. Aruljothi, P. Balaji, E. Vaishnavi, T. Pazhanivel and T. Vasuki, *J. Chem. Technol. Biotechnol.*, 2023, **98**, 1908–1917.
48 R. Jain and S. Gulati, *Vib. Spectrosc.*, 2023, **126**, 103540.
49 K. Nakamoto, *Infrared and Raman spectra of inorganic and coordination compounds, part B: applications in coordination, organometallic, and bioinorganic chemistry*, John Wiley & Sons, 2009.
50 M. Mączka, A. Gagor, B. Macalik, A. Pikul, M. Ptak and J. Hanuza, *Inorg. Chem.*, 2014, **53**, 457–467.
51 C. Akshhayya, M. K. Okla, A. A. AL-ghamdi, M. A. Abdel-Maksoud, H. AbdElgawad, A. Das and S. S. Khan, *Surf. Interfaces*, 2021, **27**, 101523.
52 A. Shah, A. A. Ashames, M. A. Buabeid and G. Murtaza, *J. Drug Delivery Sci. Technol.*, 2020, **55**, 101366.
53 A. Kumar, L. Rout, L. S. K. Achary, R. S. Dhaka and P. Dash, *Sci. Rep.*, 2017, **7**, 42975.
54 Y. Yao, Z. Huang, P. Xie, L. Wu, L. Ma, T. Li, Z. Pang, M. Jiao, Z. Liang and J. Gao, *Nat. Nanotechnol.*, 2019, **14**, 851–857.
55 N. Masunga, O. K. Mmelesi, K. K. Kefeni and B. B. Mamba, *J. Environ. Chem. Eng.*, 2019, **7**, 103179.
56 L. Guo, S. Hwang, B. Li, F. Yang, M. Wang, M. Chen, X. Yang, S. G. Karakalos, D. A. Cullen and Z. Feng, *ACS Nano*, 2021, **15**, 6886–6899.
57 W.-D. Oh, L.-W. Lok, A. Veksha, A. Giannis and T.-T. Lim, *Chem. Eng. J.*, 2018, **333**, 739–749.
58 U. Quyyum, K. Rafiq, M. Z. Abid, F. Ahmad, A. Rauf and E. Hussain, *Environ. Sci.: Water Res. Technol.*, 2023, **9**, 1147–1160.
59 N. Sasirekha, S. J. S. Basha and K. Shanthi, *Appl. Catal., B*, 2006, **62**, 169–180.
60 M. S. Hossain, H. Kabir, M. M. Rahman, K. Hasan, M. S. Bashar, M. Rahman, M. A. Gafur, S. Islam, A. Amri and Z.-T. Jiang, *Appl. Surf. Sci.*, 2017, **392**, 854–862.
61 M. Kumar, B. Meena, P. Subramanyam, D. Suryakala and C. Subrahmanyam, *Catalysts*, 2022, **12**, 1198.
62 C. Xiunan, T. Ling, C. Meifei, L. Yijun, W. Wei, L. Junhao, Z. Yanjuan, T. Gan, H. Huayu and H. Zuqiang, *Chemosphere*, 2022, **296**, 134005.
63 C. Sang, K. Chen, G. Li, S. Jin and Y. Luo, *RSC Adv.*, 2021, **11**, 7633–7643.
64 M. Z. Abid, A. Ilyas, K. Rafiq, A. Rauf, M. A. Nadeem, A. Waseem and E. Hussain, *Environ. Sci.: Water Res. Technol.*, 2023, **9**, 2238–2252.
65 S. Liang, S. Chen, Z. Guo, Z. Lan, H. Kobayashi, X. Yan and R. Li, *Catal. Sci. Technol.*, 2019, **9**, 5292–5300.
66 Q. Li, N. Luo, D. Xia, P. Huang, X. Liu, T. Odoom-Wubah, J. Huang, G. Chai, D. Sun and Q. Li, *Environ. Sci.: Nano*, 2022, **9**, 781–796.
67 K. Duan, T. Que, S. Koppala, R. Balan, B. Lokesh, R. Pillai, S. David, P. Karthikeyan, S. Ramamoorthy and I. Lekshmi, *RSC Adv.*, 2022, **12**, 16544–16553.
68 V. N. Nikolić, M. M. Vasić and D. Kisić, *J. Solid State Chem.*, 2019, **275**, 187–196.
69 A. Wang, S. Guo, M. Xu, C. Meng, H. Zhu, T. Zheng, H. Wang, K. Wang, W. Shi and X. Liu, *Appl. Catal., B*, 2023, **322**, 122117.
70 H. Lahmar, M. Benamira, L. Messaadia, K. Telmani, A. Bouhala and M. Trari, *Advances in Renewable Hydrogen and Other Sustainable Energy Carriers*, Springer, 2020, pp. 129–136.
71 A. Mehtab, S. Banerjee, Y. Mao and T. Ahmad, *ACS Appl. Mater. Interfaces*, 2022, **14**, 44317–44329.
72 H. Yang, J. Yan, Z. Lu, X. Cheng and Y. Tang, *J. Alloys Compd.*, 2009, **476**, 715–719.
73 K. Atacan, B. Topaloğlu and M. Özacar, *Appl. Catal., A*, 2018, **564**, 33–42.
74 M. Tang, F. Xia, C. Gao and H. Qiu, *Int. J. Hydrogen Energy*, 2016, **41**, 13058–13068.
75 T. Zhang, H. Zhu and J.-P. Croue, *Environ. Sci. Technol.*, 2013, **47**, 2784–2791.
76 G. Liu, P. Niu, C. Sun, S. C. Smith, Z. Chen, G. Q. Lu and H.-M. Cheng, *J. Am. Chem. Soc.*, 2010, **132**, 11642–11648.
77 R. M. Ali, M. R. Elkatory and H. A. Hamad, *Fuel*, 2020, **268**, 117297.
78 F. Saleem, M. Z. Abid, K. Rafiq, A. Rauf, K. Ahmad, S. Iqbal, R. Jin and E. Hussain, *Int. J. Hydrogen Energy*, 2023, **52**, 305–319.
79 Z. H. N. Al-Azri, W.-T. Chen, A. Chan, V. Jovic, T. Ina, H. Idriss and G. I. N. Waterhouse, *J. Catal.*, 2015, **329**, 355–367.
80 M. Jalil, K. Rafiq, M. Z. Abid, A. Rauf, S. Wang, S. Iqbal and E. Hussain, *Nanoscale Adv.*, 2023, **5**, 3233–3246.
81 E. Hussain, I. Majeed, M. A. Nadeem, A. Badshah, Y. Chen, M. A. Nadeem and R. Jin, *J. Phys. Chem. C*, 2016, **120**, 17205–17213.
82 E. Hussain, I. Majeed, M. A. Nadeem, A. Iqbal, Y. Chen, M. Choucair, R. Jin and M. A. Nadeem, *J. Environ. Chem. Eng.*, 2019, **7**, 102729.
83 M. Sabir, K. Rafiq, M. Z. Abid, U. Quyyum, S. S. A. Shah, M. Faizan, A. Rauf, S. Iqbal and E. Hussain, *Fuel*, 2023, **353**, 129196.
84 M. Z. Abid, A. Tanveer, K. Rafiq, A. Rauf, R. Jin and E. Hussain, *Nanoscale*, 2024, **16**, 7154–7166.
85 K. U. Sahar, K. Rafiq, M. Z. Abid, A. Rauf, U. ur Rehman, M. A. Nadeem, R. Jin and E. Hussain, *Colloids Surf., A*, 2023, **674**, 131942.